

## APPLIED RESEARCH

# MILS and HILS Analysis of Power Management System for UAVs

SUNGHUN JUNG<sup>1</sup>, (Member, IEEE), AND YOUNG-JOON KIM<sup>2</sup>, (Member, IEEE)

<sup>1</sup>Department of Smart Mobile Convergence System, College of Engineering, Chosun University, Gwangju 61452, Republic of Korea

<sup>2</sup>Department of Electronic Engineering, College of IT Convergence, Gachon University, Seongnam 13120, Republic of Korea

Corresponding author: Young-Joon Kim (youngkim@gachon.ac.kr)

This work was supported by the Research Fund from Chosun University, in 2021, under Grant K208419003.

**ABSTRACT** This study developed four different power management system (PMS) prototypes based on the most popular mission computers used for offboard mission operation by the PX4 (open-source UAV flight controller software platform) user community for a photovoltaic (PV)-powered unmanned aerial vehicle (UAV). The four PMS prototypes were compared in terms of operational performance through an analysis of data obtained from a model-in-the-loop simulation and hardware-in-the-loop simulation using charging and discharging current patterns, saved from an outdoor PV panel power generation and multirotor UAV flight tests, respectively, under varying environmental temperature. Two types of simulations were performed, depending upon the additional placement of a supercapacitor in parallel with a Li-ion battery pack, to verify the effectiveness of the Li-ion battery pack life extension through high current shock mitigation. Simulation results demonstrated that the application of a supercapacitor in parallel with a Li-ion battery pack resulted in poor performance indicated by in-flow current fluctuation deviation measurements during the end of the constant current and constant voltage charging process. Moreover, this behavior was confirmed to be mainly because of the inherent high C-rate performance capability of the Li-ion battery pack compared to the supercapacitor. Among the four PMS candidates, under 25 °C without supercapacitor, Jetson TX2 was found to exhibit the best functionality in terms of power management (0.41 W of power fluctuation deviation), whereas AMega yielded the best functionality in terms of energy management (1165.4 s of flight time).

**INDEX TERMS** Energy management, hardware-in-the-loop simulation, model-in-the-loop simulation, power management system, unmanned aerial vehicle.

## I. INTRODUCTION

### A. BACKGROUND

The use of unmanned aerial vehicles (UAVs) has recently garnered increased attention. Although active work is ongoing toward advancing the field of UAV utilization, most efforts on the methods of increasing the flight time to enable the actual use of UAVs have been limited to the development of battery cells with a high energy density.

When considering the enhancement of the endurance of various types of UAVs, the following key aspects are essential: (1) low energy usage during flight assisted using a low-drag-inducing streamlined fuselage; (2) an optimized

flight path that exploits the ascending airflow around thermal updrafts; and (3) the use of power sources exhibiting a high energy density. Unfortunately, a low-priced and low-altitude UAV does not usually possess the three listed aspects; therefore, additional methods are required to realize such UAVs that also possess long endurance.

In this context, a fuel cell (FC) system cannot be exploited to enhance the flight time because it can only carry a limited amount of hydrogen fuel, which cannot be easily replenished during flight, thus rendering everlasting flight without landing impossible. Consequently, this study utilized a photovoltaic (PV) energy source with a power management system (PMS), where the latter manages power flows among the PV modules, battery pack, and supercapacitor to support the power load required by the UAV's motors. Moreover,

The associate editor coordinating the review of this manuscript and approving it for publication was Abderrahmane Lakas<sup>1</sup>.

a supercapacitor was added to test whether it indeed alleviated sudden high loads affecting the Li-ion battery pack, thereby enhancing flight endurance. Four types of commercial embedded boards were utilized as the mission computer (MC) on the PMS platform board, namely, the Arduino Mega (AMega), Raspberry Pi 3 Model B (RPi 3B), NVIDIA Jetson Nano, and NVIDIA Jetson TX2—these are the most popular MCs used in combination with a Pixhawk flight controller.

The NVIDIA Jetson TX2 has garnered attention because of its relatively small size and high computing power. When building the prototypes using one of the listed MCs, board-to-board stacking was employed because of the convenience of replacement in case the MC malfunctioned.

To develop a UAV with long endurance and safety as key factors, this study explored two primary research subjects: energy and power management, both of which have been actively studied since the mid-2000s. Neither of these factors can be neglected if a safe UAV deployment of a long duration is to be achieved. In this study, the exploration of energy management focused on strategic methods to achieve a longer flight time. In contrast, the exploration of power management was focused more on determining which systematic perspective can achieve a controllable rate of energy consumption. Specifically, energy management addresses methodological approaches, including path planning and endurance estimation, whereas power management addresses systematic approaches, including the power management system and control algorithm development, and the testing thereof.

### B. ENERGY MANAGEMENT ASPECT

With respect to energy management path planning, Huang et al. presented energy-optimal path planning based on receding horizon control (RHC) and particle swarm optimization (PSO) for the target tracking mission, using a fixed-wing UAV [1]. Later, Huang et al. presented energy-optimal path planning based on PSO and a novel penalty function for the stationary target mission, using a fixed-wing UAV [2]. Further, Huang et al. presented a 3D trajectory model, which considered factors such as UAV energy consumption, PV power generation, eavesdropping, and no-fly zones based on a rapidly-exploring random tree (RRT) method to ultimately construct secure wireless communication [3]. Wu et al. presented a whale optimization algorithm (WOA) with an adaptive chaos-Gaussian switching solving strategy to obtain UAV trajectories [4]. Wu et al. later presented energy management strategies utilizing solar energy, potential energy, and wind vectors to accomplish a long-endurance target tracking mission [5]. Further, Wu et al. presented the endurance map for generating energy-efficient UAV trajectories [6]. He et al. presented a fuzzy logic-based energy management PMS with hardware-in-the-loop simulation (HILS) verification [7]. Tazvinga et al. presented a model predictive control technique, PV-wind-diesel-battery PMS [8].

With respect to energy management endurance estimates, Huang et al. presented a graphical-method-based UAV endurance estimate [9].

### C. POWER MANAGEMENT ASPECT

With respect to power management algorithms, Zhang et al. presented an online fuzzy power management strategy using only a single programmable DC–DC converter to manage the current flow of both an FC and a battery pack [10]. Further, Zhang et al. presented a fuzzy state machine (FSM) power management strategy with an online potential to manage power flow among an FC, PV modules, and a battery pack [11]. Mobariz et al. presented the results of simulations based on the gradient descent multi-parameter-optimization technique for a PID controller of a DC–DC buck converter to manage power flows between an FC and battery pack [12]. Shiau et al. presented the results of simulations of a fuzzy logic-based, voltage-regulated maximum power point tracking (MPPT) system to control power flows between PV modules and a battery pack [13]. Gong et al. presented a HILS test bench based on an open-source flight simulator and demonstrated electricity flows between an FC and battery pack in the simulation world [14].

Further, Gong et al. presented flight test results of a PMS controlling the power flows among an FC, battery pack, and a supercapacitor comprising a feasibility study into the usefulness of adding a supercapacitor [16]. Malaver et al. presented operational results for a solar-powered UAV (SUAV) used for environmental gas sensing and employing two MPPT boards and a battery charger, obtained employing the power path manager technique [17]. Oettershagen et al. presented all the fundamental design work required for developing an SUAV exhibiting a flight time and distance of 81 h and 2,338 km, respectively, thus achieving a world record. They incorporated a PMS that managed the energy flow and monitored overall and cell-level charge states [18]. Shiau and Ma presented an SUAV with an auto-ranging buck-boost DC–DC power converter with MPPT, battery charging, and voltage regulation functions [19]. Stroman et al. demonstrated a UAV powered by both PV and an FC, incorporating FC propulsion, soaring, solar harvesting, and optimal path planning [20]. Yang et al. developed an FC system containing a polymer electrolyte fuel cell (PEFC) and a lithium polymer (Li-po) battery pack connected in parallel, where the latter was used for passive control using only a single manually-operated relay switch [21].

Energy management and power management were addressed simultaneously in a critical review by Boukoberine et al., which focused on power supply configurations and energy management systems being used for developing hybrid power architecture [22]. Lei et al. performed a literature survey of the energy management strategy (EMS) for a PMS, which is mainly divided into offline and online control algorithms, and implemented it on a UAV with the aim of realizing long endurance [23].

### D. PMS ROBUSTNESS ASPECT

While energy and power management have garnered significant attention, the robustness of energy and power management hardware has rarely been discussed in studies.

Most studies highlighted above examined only the energy-flow- or power-flow-related technologies by evaluating their software algorithm or hardware system through experiments conducted at room temperature; in contrast, varying environmental temperature, where such experiments are performed, is often neglected.

However, because of the characteristics of a multi-layered hardware printed circuit board (PCB), wherein various micro parts are electrically and mechanically fastened and connected, the PMS is typically sensitive to harsh external temperature changes, which can result in unintended malfunctions. In other words, changes in temperature and relative humidity (RH) accompanying an increase in the operating altitude of the UAV can adversely affect the PCB by considerably increasing leakage current at sodium chloride concentrations and resulting in the formation of tin whiskers and hillocks, which can result in a short circuit [24].

Aside from the extreme case of a short circuit, excessively high or low ambient temperatures can affect the performance of the PMS circuit, depending on factors such as the circuit design, circuit component placement, and PCB material [25]. Although this problem can be solved via the addition of a heat dissipation or generation device to the PMS, the sensitivity of UAVs to payload weight renders this a less desirable solution.

As previously explained, serious system malfunctions (or even minor system errors occurring for a short time) can cause UAVs to crash to the ground owing to movements at high speeds and altitudes. Therefore, there is a need for a robust system verification process prior to incorporating new system components into a UAV. Consequently, this study aimed to investigate the effects of environmental temperature on the PMS hardware in cases where a UAV operates for several hours. The objective was to determine the robustness of the PMS upon exposure to hazardous environmental temperatures.

Additional environmental tests were performed because the PMS was developed via the addition of several sub-components, in addition to the microcontroller. This is the reason system developers in the market sequentially perform indoor (1) model-in-the-loop simulation (MILS), (2) software-in-the-loop simulation (SILS), (3) processor-in-the-loop simulation (PILS), and (4) HILS, and outdoor tests for robust system development [26].

To optimize both the energy and power management strategies at the troposphere region, where low-altitude and long-endurance (LALE) UAVs typically fly, a power management board that is robust in both low and high environmental temperatures must be developed.

In this study, the temperatures  $-10\text{ }^{\circ}\text{C}$  and  $40\text{ }^{\circ}\text{C}$  were chosen because they represent the environmental temperature at an altitude under 3 km (underneath the air traffic) where most of the system operations perform.

### E. PMS DEVELOPMENT ASPECT

Shiau et al. presented the results of a solar power management system for managing power flows between PV modules,

a battery pack, and motors with the MPPT, battery management system (BMS), and a power converter using an experimental UAV [27]. Bystrov et al. presented processes of PMS modeling and simulation based on MATLAB and real PMS prototype design for UAV hybrid systems with a gasoline internal combustion engine [28].

### F. MAIN CONTRIBUTIONS

Our focus of this manuscript can be divided into two parts.

(1) For the MILS, we set up simplified electrical circuit models of subsystems including the PV modules, battery pack, supercapacitor, and motor with additional parameter estimation processes using MATLAB/Simulink to precisely mimic the real hardware performance;

(2) For the HILS, the four PMS prototypes were tested under high ( $40\text{ }^{\circ}\text{C}$ ) and low ( $-10\text{ }^{\circ}\text{C}$ ) ambient temperatures with respect to the presence or absence of a supercapacitor to analyze hardware robustness in two aspects; 1) fluctuation deviation of power flow and 2) flight time.

### G. ARTICLE ORGANIZATION

The remaining article is organized as follows. In Section II, detailed information on the PMS (overview, comparison of four PMS prototypes, principle of operation, and circuit design) is presented. The MILS and HILS experimental setup and the corresponding results are presented in Sections III and IV, respectively. Further, the comparison of the MILS and HILS results is presented in Section V. Finally, concluding remarks and suggestions for future work are presented in Section VI.

## II. PMS

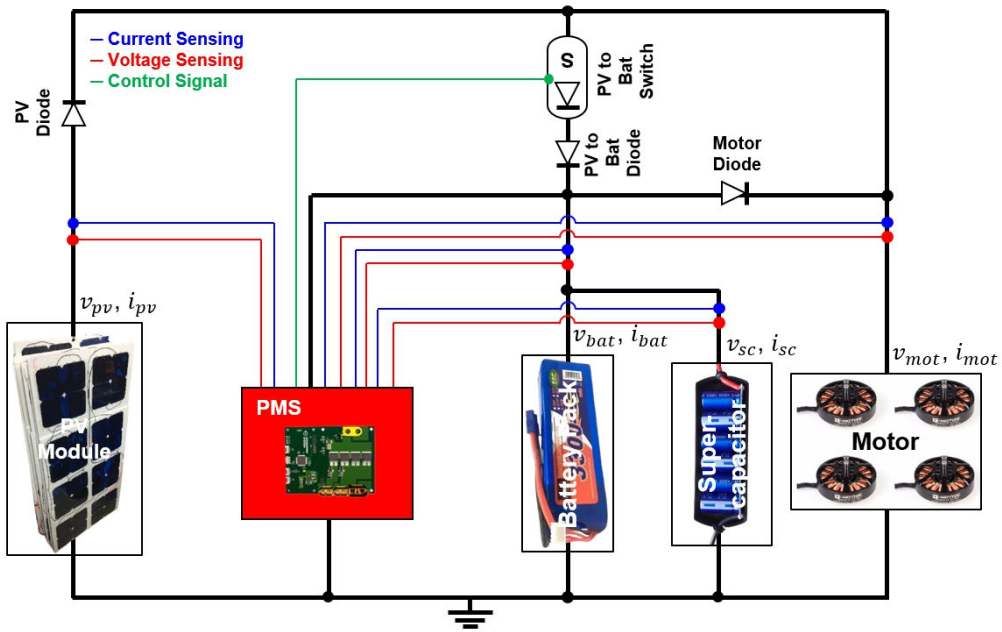
### A. OVERVIEW

As a PMS is installed in the UAV alongside many other components, particularly a BMS, all the possible interconnections among the components must be analyzed. Because many components are co-related and shared a common electrical ground, current and voltage accumulation, peaks, fluctuation, etc. must be paid attention to such that possible malfunctions are avoided (Fig. 1(a)). We can achieve the overall power related system safety with the list of major functions of both a PMS and a BMS (Fig. 1(b)).

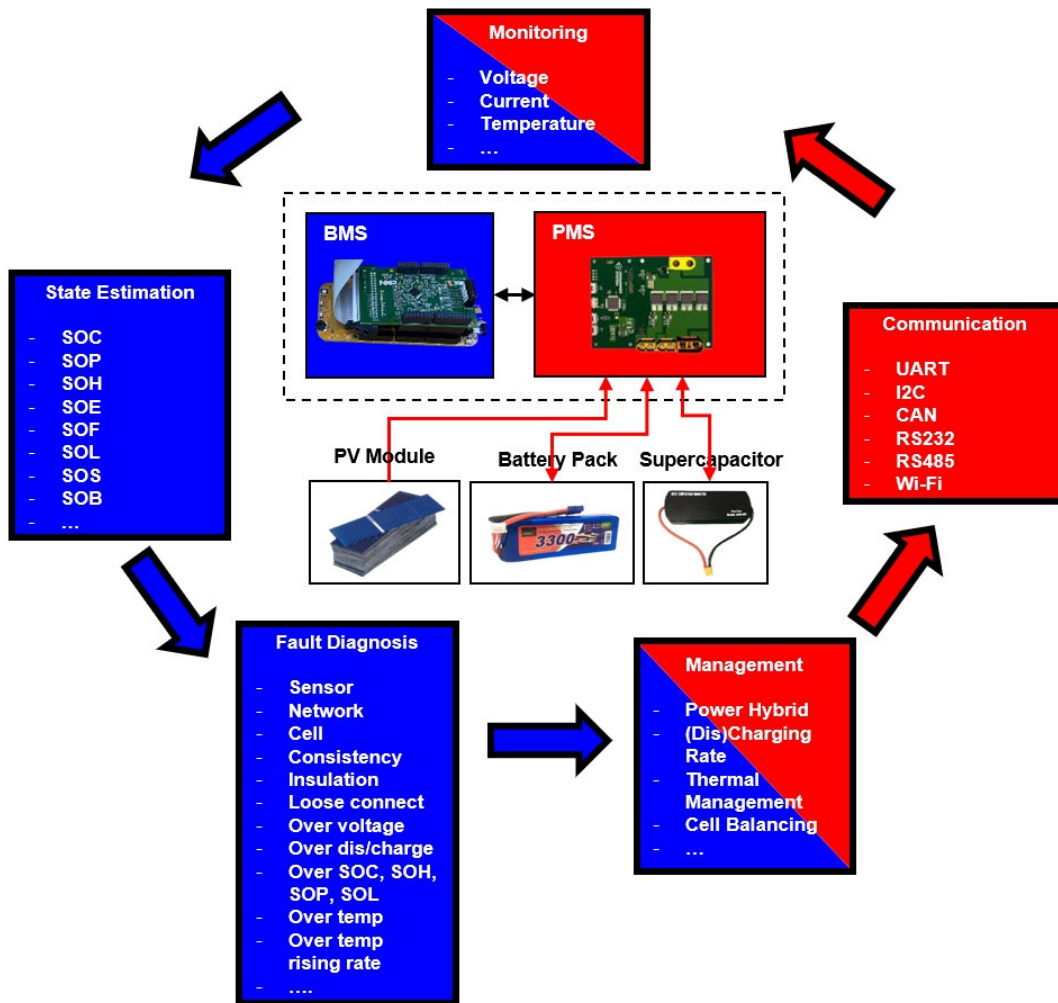
In total, four PMS prototypes were developed, based on an AMega, RPi 3B, NVIDIA Jetson Nano, and NVIDIA Jetson TX2, as shown in Appendix A.

Each PMS had four ports that were used for connecting a battery pack, supercapacitor, PV modules, and UAV. When performing an indoor HILS test, the port for the PV modules was connected to the charger (DC power supply), that for the UAV was connected to the discharger (DC electronic load), the one for the battery pack was connected to a real battery pack, and that for the supercapacitor was connected to a real supercapacitor.

All four PMSs used the same PMS operating code, referred to as either `powermanager.ino` or `powermanager.py`; however,



(a)



(b)

FIGURE 1. Conceptual diagram of the PMS (highlighted in red): (a) electrical interconnection, (b) list of major functions.

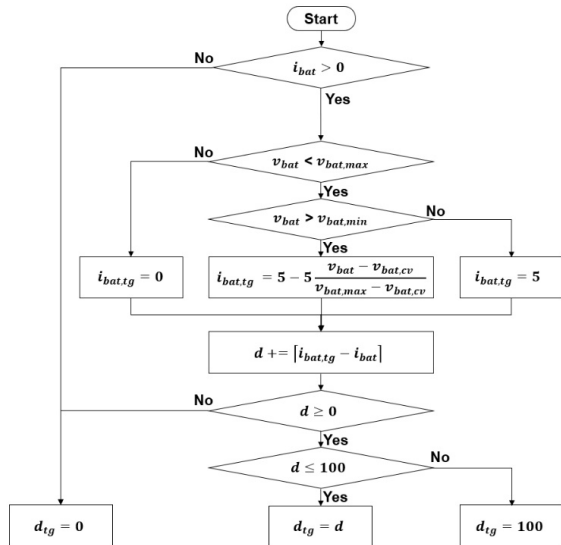


FIGURE 2. Conceptual diagram of the PMS operation.

the codes were slightly modified depending on each platform because of the different pin mappings. The operating code of the PMS with an AMega was saved as powermanager.ino and those of the other three PMSs were saved as powermanager.py.

Further, one of the commercial embedded boards was used as the main computer for each PMS to facilitate its use as an MC and enable communication between the PMS and a flight controller, particularly a Pixhawk, through the micro air vehicle link (MAVLINK) protocol. Thus, a PMS should wirelessly communicate with a GCS, and all four PMSs can communicate over Wi-Fi communication.

**B. COMPARISON OF PMS PROTOTYPES**

To control the amount of current flow, the MOSFET switch shown in Fig. 1(a) was installed and managed by controlling pulse width modulation (PWM) signals generated by an MC.

Four types of commercial embedded boards were considered for use as an MC, and the detailed specifications of each MC are listed in Appendix A alongside those from other studies.

**C. PRINCIPLE OF OPERATION**

The main operating principle of the PMS was the gathering of energies from various sources and guiding the power flow to supply motors attached to the UAV.

A conceptual diagram of the PMS operation is shown in Fig. 2. The charging current flow to charge the battery pack should be properly managed to prevent battery pack swelling and avoid overly slow charging. The amount of charging current can be managed by varying the MOSFET duty cycle. Because a 3.3 Ah battery pack was used, the charging current was limited to the range of 0–5 A by varying the duty cycle from 0 to 100 %.

The same operation principle and setup values shown in Fig. 2 and Table 1 are applied to all four types of PMSs for the performance comparison analysis.

TABLE 1. List of variables used in PMS operation.

Symbol	Definition	Unit	Value
$v_{bat,max}$	maximum allowable battery pack voltage	V	17.2
$v_{bat,min}$	minimum allowable battery pack voltage	V	13
$v_{bat,cv}$	battery pack voltage when CV mode starts	V	16.4
$v_{bat}$	battery pack voltage	V	-
$i_{bat,tg}$	target battery pack charging current	A	-
$i_{bat}$	battery pack current	A	-
$d$	calculated PWM duty cycle	%	-
$d_{tg}$	target PWM duty cycle	%	-

TABLE 2. List of variables used in PMS modeling.

Symbol	Definition	Unit	Value
$P_{mot}$	motor power	W	-
$P_{pv}$	PV power at load end	W	-
$P_{bat}$	battery pack power	W	-
$P_{sc}$	supercapacitor power	W	-
$i_{mot}$	motor current	A	-
$i_{pv}$	PV current at load end	A	-
$i_{bat}$	battery pack current	A	-
$i_{sc}$	supercapacitor current	A	-
$v_{mot}$	motor voltage	V	-
$v_{pv}$	PV voltage at load end	V	-
$v_{bat}$	battery pack voltage	V	-
$v_{sc}$	supercapacitor voltage	V	-

**D. CIRCUIT DESIGN**

Circuit designs of the AMega, RPi 3B, NVIDIA Jetson Nano, and NVIDIA Jetson TX2 based PMS prototypes were drawn using the Fritzing open-source software. To compare the performance, the same current sensor, voltage sensor, and MOSFET were used in the PMS prototypes.

Most of the circuit diagrams were intentionally designed to be the same or, at least, similar for conducting the performance comparison analysis.

**III. MILS**

**A. SIMULATION SETUP**

By simplifying the internal power flows of the PMS, simple mathematical equations can be derived as follows:

$$P_{mot} = P_{pv} + P_{bat} + P_{sc} \tag{1}$$

$$i_{mot}v_{mot} = i_{pv}v_{pv} + i_{bat}v_{bat} + i_{sc}v_{sc} \tag{2}$$

$$i_{mot} = i_{pv} + i_{bat} + i_{sc}, \tag{3}$$

where PV, BAT, and SC represent the PV modules, battery pack, and supercapacitor, respectively. The variables are defined in Table 2. Further, detailed mathematical modeling of the PV modules, battery pack, supercapacitor, and motor is shown below.

Throughout the end of this Section, simplified electrical circuit models were set for subsystems including the PV modules, battery pack, supercapacitor, and motor, and subsequently, the parameter estimation process was performed with previously obtained experimental results. Consequently,

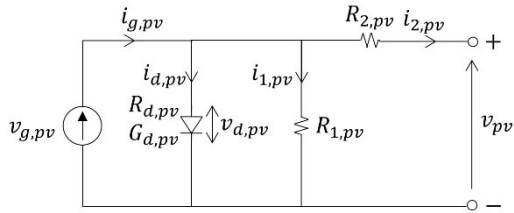


FIGURE 3. PV cell ECM.

TABLE 3. List of variables used in PV module modeling.

Symbol	Definition	Unit	Value
$i_{g,pv}$	generated PV current	A	-
$i_{d,pv}$	diode current	A	-
$i_{1,pv}$	current across resistor $R_1$	A	-
$i_{2,pv}$	current across resistor $R_2$ ( $= i_{pv}$ )	A	-
$R_{1,pv}$	resistance 1	$\Omega$	22734
$R_{2,pv}$	resistance 2	$\Omega$	1.7327e-6
$R_{d,pv}$	diode ON resistance	$\Omega$	5077.4
$v_{d,pv}$	diode voltage	V	-
$G_{d,pv}$	diode OFF conductance	$1/\Omega$	1e-8
$\eta_{mppt}$	efficiency of the MPPT	no unit	1
$\eta_{pv}$	efficiency of the PV modules	no unit	1
$\alpha$	solar incidence angle	rad	0
$P_{g,pv}$	generated PV power	W	-

with the estimated parameters, each subsystem was combined into one model to simulate and analyze the performance of the overall PMS.

### 1) PV MODULES

An electrical diagram of the PV cell and the solar incidence angle on PV modules are shown in Fig. 3.

Considering the piecewise linear diode model and a forward biased situation, the simplified mathematical model of the PV modules can be derived using the following equations:

$$i_{g,pv} = i_{d,pv} + i_{1,pv} + i_{2,pv} \quad (4)$$

$$i_{g,pv} = i_{d,pv} + i_{1,pv} + i_{pv} \quad (5)$$

$$i_{g,pv} = \frac{v_{d,pv} (1 - R_{d,pv} G_{d,pv})}{R_{d,pv}} + \frac{v_{pv} + R_{2,pv} i_{2,pv}}{R_{1,pv}} + i_{pv} \quad (6)$$

$$P_{g,pv} = v_{g,pv} i_{g,pv} \quad (7)$$

$$P_{pv} = \eta_{mppt} \eta_{pv} v_{pv} i_{pv} \cos \alpha, \quad (8)$$

where the variables and their estimated parameter values are defined in Table 3 [11], [30].

### 2) BATTERY PACK

An electrical diagram of the battery pack is shown in Fig. 4.

A simplified mathematical model of the battery pack can be derived as

$$v_{bat} = v_{oc,bat} - i_{bat} R_{0,bat} (z) - v_{1,bat} \quad (9)$$

$$v_{1,bat} = i_{bat} R_{1,bat} (z) \left( 1 - e^{-t/\tau_{1,bat}(z)} \right) \quad (10)$$

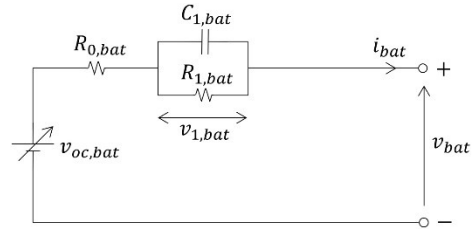


FIGURE 4. One ladder battery ECM.

TABLE 4. List of variables used in battery pack modeling.

Symbol	Definition	Unit	Value
$v_{oc,bat}$	OCV	V	-
$R_{0,bat}$	resistance 0	$\Omega$	[0.01, 0.01, 0.01, 0.010054, 0.027667, 0.032698, 1.8712e-4, 6.1044e-3, 3.3719e-3, 2.0905e-3, 0.19919]
$R_{1,bat}$	resistance 1	$\Omega$	[0.005, 0.005, 0.005, 5.0203e-3, 5.9909e-3, 2.4429e-2, 1.8135e-3, 1.5798e-3, 1.9319e-2, 2.7816e-3, 2.5381e-4]
$C_{1,bat}$	capacitance 1	F	[10000, 10000, 10000, 10002, 5914.1, 0.84908, 18788, 3804, 8047.1, 1621.6, 2377.2]
$\tau_{1,bat}$	time constant 1	s	-
$z$	SOC	%/100	-
$Q_{init}$	initial battery capacity	Ah	-
$Q_{norm}$	current battery capacity	Ah	-
$\eta_{bat}$	battery efficiency	no unit	-

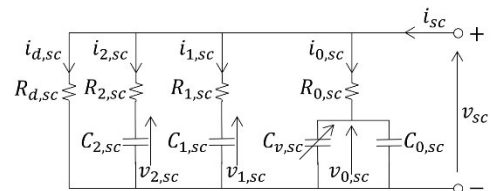


FIGURE 5. Two-branch supercapacitor ECM.

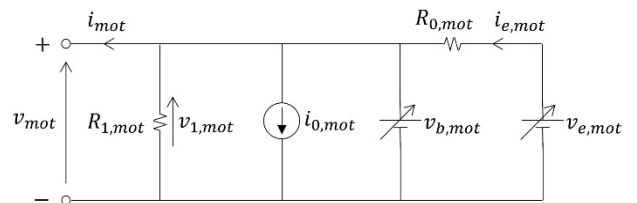


FIGURE 6. Four-constant motor ECM.

$$\tau_{1,bat} = R_{1,bat} C_{1,bat} \quad (11)$$

$$z = Q_{init} + \eta_{bat} \frac{i_{bat}}{Q_{norm}} \quad (12)$$

$$P_{bat} = v_{bat} i_{bat}, \quad (13)$$

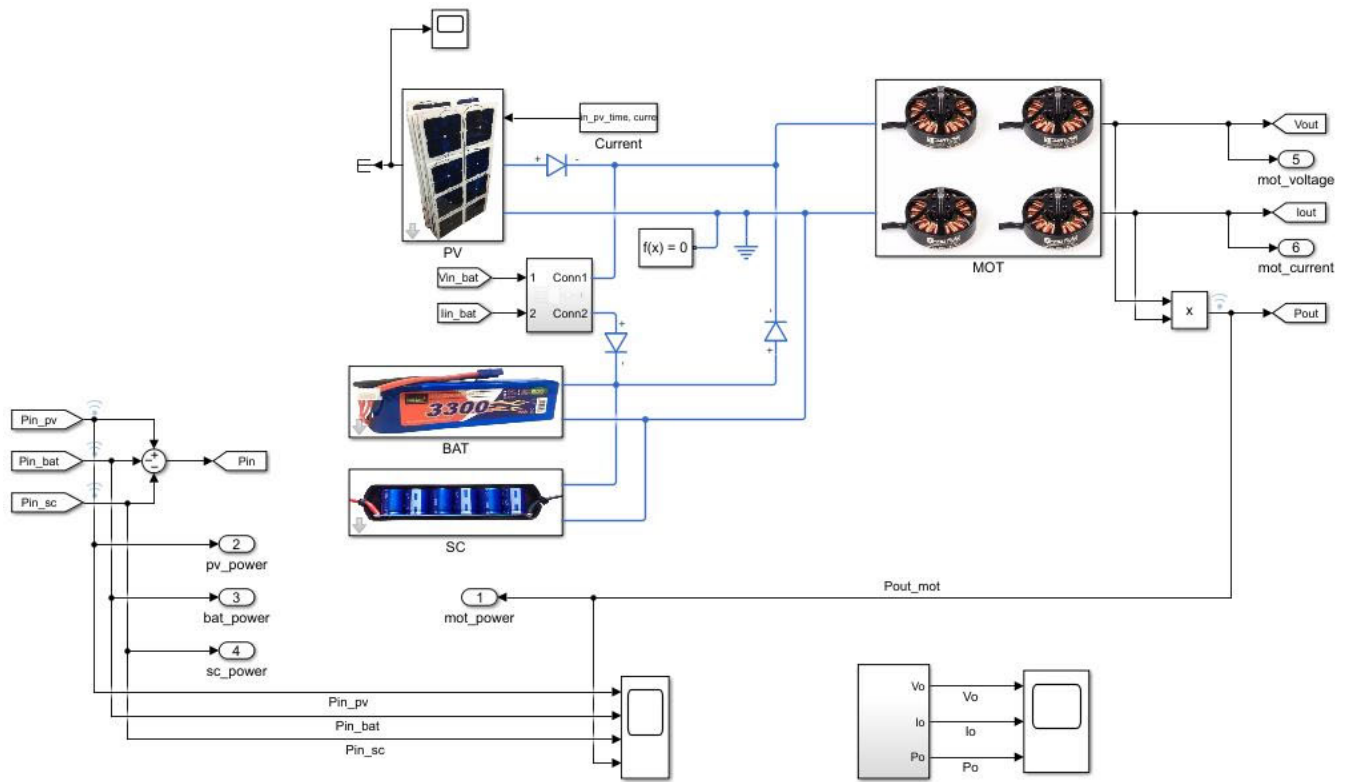


FIGURE 7. Combined ECMs of the PV modules, a battery pack, a supercapacitor, and motors.

TABLE 5. List of variables used in supercapacitor modeling.

Symbol	Definition	Unit	Value
$v_{n,sc}$	voltage across $C_{n,sc}$	V	-
$N_{s,sc}$	number of supercapacitors in series	no unit	-
$N_{p,sc}$	number of supercapacitors in parallel	no unit	-
$i_{n,sc}$	current across resistor $R_{n,sc}$	A	-
$i_{d,sc}$	current across resistor $R_{d,sc}$	A	-
$R_{0,sc}$	resistance 0	$\Omega$	1.1031e+6
$R_{1,sc}$	resistance n	$\Omega$	1.7491e+6
$R_{2,sc}$	resistance n	$\Omega$	222.1
$R_{d,sc}$	self-discharge resistance	$\Omega$	5.1258e+6
$C_{0,sc}$	capacitance 0	F	48.958
$C_{1,sc}$	capacitance 1	F	37.142
$C_{2,sc}$	capacitance 2	F	8.5657e-3
$k_{0,sc}$	voltage-dependent capacitance gain	no unit	38.259
$n$	branch number ( $\in \{0, 1, 2\}$ )	no unit	-

where the variables and their estimated parameter values are defined in Table 4 [31].

### 3) SUPERCAPACITOR

An electrical diagram of the supercapacitor is shown in Fig. 5.

With the positive voltage across the capacitor,  $C_{0,sc}$ , a simplified mathematical model of the supercapacitor can be derived as follows:

$$v_{n,sc} = \frac{v_{sc}}{N_{s,sc}} - i_{n,sc}R_{n,sc} \quad (14)$$

TABLE 6. List of variables used in motor modeling.

Symbol	Definition	Unit	Value
$v_{e,mot}$	energy-source voltage	V	-
$v_{b,mot}$	back-EMF voltage	V	-
$v_{1,mot}$	voltage across $R_{1,mot}$	V	-
$R_{0,mot}$	resistance occurred by esc and winding	$\Omega$	2.9185
$R_{1,mot}$	resistance occurred by windage and eddy current	$\Omega$	1e-6
$i_{e,mot}$	energy-source current	A	-
$i_{0,mot}$	no-load current at zero energy-source voltage	A	0.20002
$N$	Rotational speed of motor	RPM	1000
$K_v$	RPM/volt constant	no unit	380.21
$\eta_{mot}$	motor efficiency	no unit	1

$$i_{0,sc} = (C_{0,sc} + k_{0,sc}v_{0,sc}) \frac{dv_{0,sc}}{dt} \quad (15)$$

$$i_{1,sc} = C_{1,sc} \frac{dv_{1,sc}}{dt} \quad (16)$$

$$i_{2,sc} = C_{2,sc} \frac{dv_{2,sc}}{dt} \quad (17)$$

$$i_{sc} = N_{p,sc} \left( i_{0,sc} + i_{1,sc} + i_{2,sc} + \frac{v_{sc}}{R_{d,sc}} \right) \quad (18)$$

where the variables and their estimated parameter values are defined in Table 5 [32].

### 4) MOTOR

An electrical diagram of the motor is shown in Fig. 6.

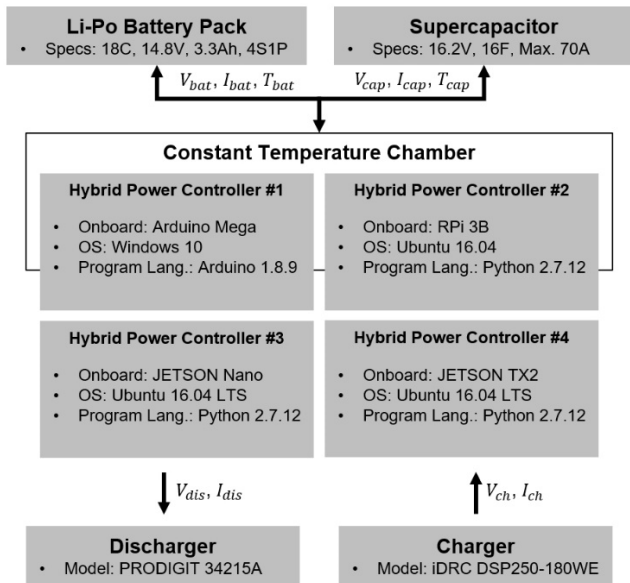


FIGURE 8. Conceptual diagram of experimental setup.

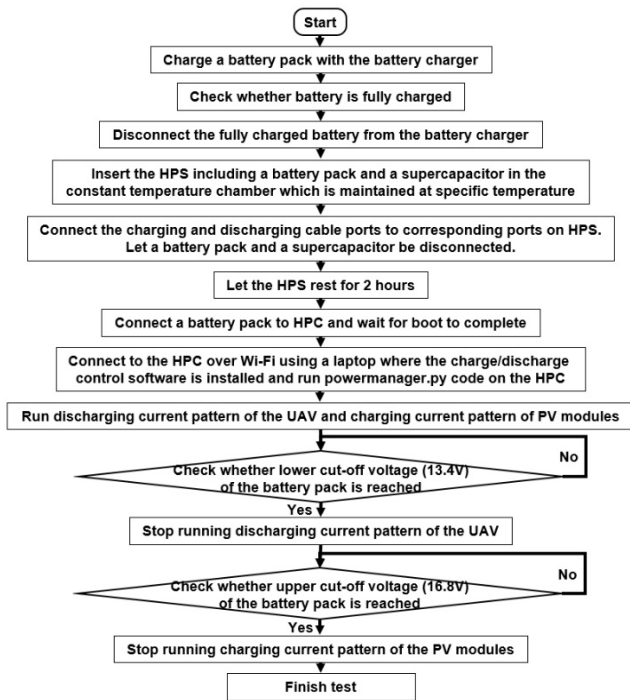


FIGURE 9. Conceptual diagram of the test procedure.

A simplified mathematical model of the motor can be derived as

$$v_{mot} = v_{b,mot} = v_{e,mot} - i_{e,mot}R_{0,mot} \quad (19)$$

$$v_{b,mot} = \frac{N}{K_v} \quad (20)$$

$$i_{mot} = i_{e,mot} - i_{0,mot} - \frac{v_{1,mot}}{R_{1,mot}} \quad (21)$$

$$P_{mot} = \eta_{mot}v_{mot}i_{mot}, \quad (22)$$

where the variables and their estimated parameter values are defined in Table 6 [33].

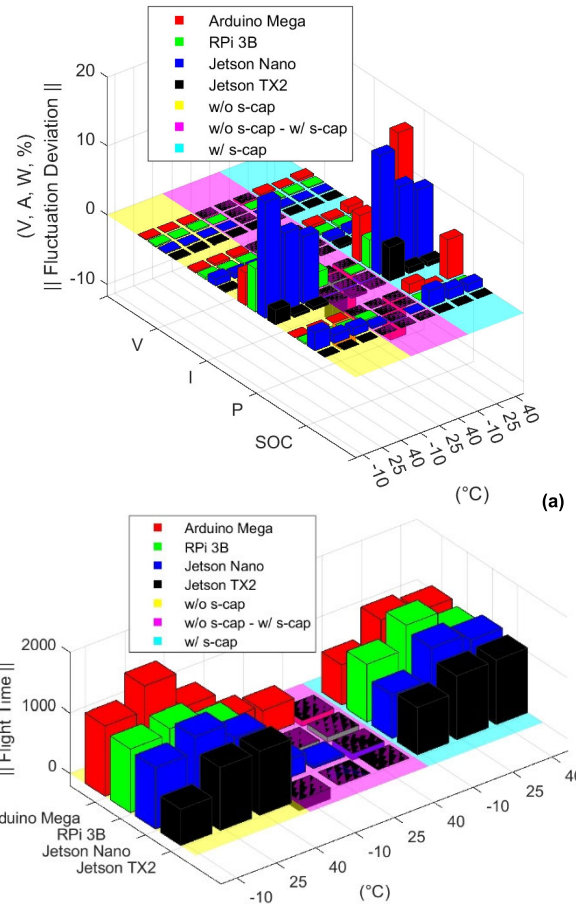


FIGURE 10. Comparison plot for tests w/o and w/ supercapacitor: (a) fluctuation deviation, (b) flight time.

## 5) COMBINATION

An electrical diagram of the overall combined ECMs, including PV modules, battery pack, supercapacitor, and motors, and the implemented Simulink model are shown in Section IV.

## B. SIMULATION RESULTS

The MILS result for voltage, current, power, and SOC for the PV modules, battery pack, supercapacitor, and motors were drawn for the power interflow analysis, and it was overlapped with the HILS result, as shown in Section V.

## IV. HILS

### A. SIMULATION SETUP

To emulate the power supply from the PV modules and the power load by a motor ESC during real flights in the indoor environment, the outdoor hovering flight was first performed using a quadrotor UAV while the PV modules were connected. Subsequently, the PV modules, quadrotor UAV, and battery pack were connected to one of the PMS prototypes, and the current flow of each connection was saved once the hovering flight began. Thereafter, a portion of the saved current profiles was extracted and used for the HILS. The indoor emulation was prepared with a DC power



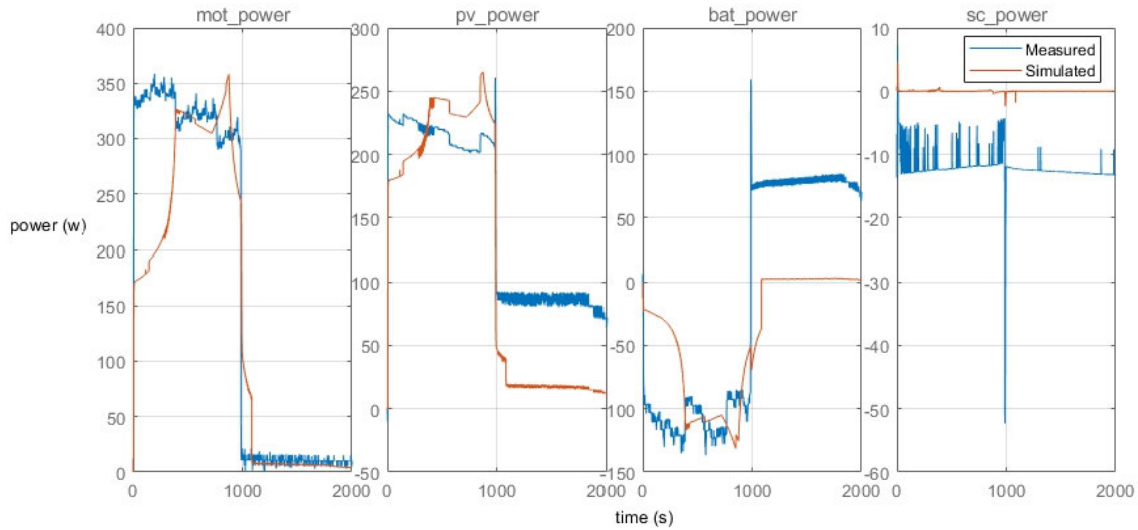


FIGURE 11. MILS and HILS comparison: (a) experiment result, (b) power.

supply, DC electronic load, constant temperature chamber, and software GUIs.

A conceptual diagram indicating the manner in which the DC power supply, DC electronic load, constant temperature chamber, battery pack, supercapacitor, and PMS were interconnected is shown in Fig. 7 and its experimental setup is shown in Fig. 8.

A flowchart mapping the overall test procedures, starting from the preparation of a fully charged battery pack to the end of the charging and discharging cycle, is shown in Fig. 9.

To test the manner in which the PMS behaved under a variety of actual environmental temperatures, the entire PMS—including the PMS, battery pack, and supercapacitor—was placed inside the constant temperature chamber and soaked at different temperatures: -10, 25, and 40 °C, for two hours.

Regarding the in-depth analysis of the role of the battery pack during the HILS test, a MATLAB/Simulink-based state of charge (SOC) estimation model was developed by extracting equivalent circuit model (ECM) parameters using hybrid pulse power characterization (HPPC) current patterns [31].

### B. SIMULATION RESULTS

Each of the four PMS prototypes was tested under three different environmental temperatures, as shown in Appendix B. The experimental results for voltage, current, power, and SOC for the PV modules, battery pack, UAV, and supercapacitor were obtained for the power interflow analysis.

The previously listed experimental results shown in Appendix B were summarized in terms of two quantities: fluctuation deviation and flight time, as presented in Appendix C and Figs. 10. The part of the CV charging mode was used rather than the discharging mode for the fluctuation deviation analysis because most of the fluctuations were caused by fluctuations in the battery pack charging current.

Here, the fluctuations in the battery pack charging current were mostly caused by the MOSFET operation that

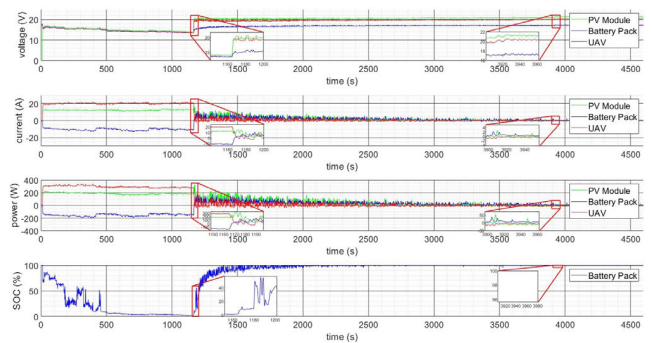


FIGURE 12. Result for Arduino-Mega-based PMS (w/o supercapacitor).

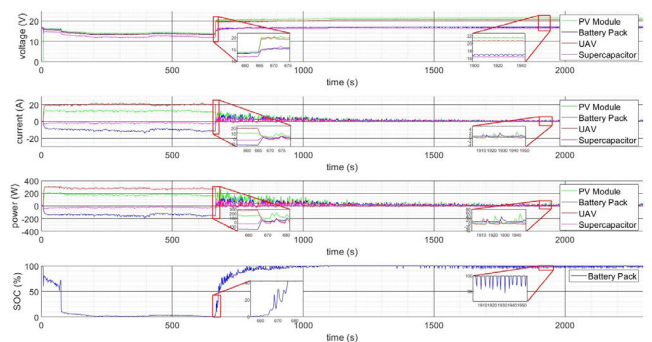


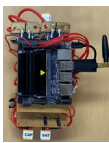
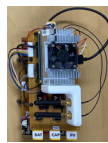

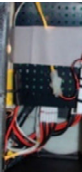




FIGURE 13. Result for Arduino-Mega-based PMS (w supercapacitor).

controlled the amount of current flow into the battery pack from the PV modules.

Figure 10(a) shows the graphical representation of the battery column in Appendix C. Table 8, whereas Fig. 10(b) shows the visual representation of Appendix C. Table 13. Certain caution is required while using the results presented in Appendix B because they were obtained from indoor HILS tests rather than from real flight tests. Nevertheless, the data are valuable for further analyses, as presented below.

TABLE 7. Companion computer comparison.

	PMS based on				Reference [15]	Reference [29]	Reference [20]	Reference [16]	
	AMega	RPi 3B	Jetson Nano	Jetson TX2 (w/ Orbbity)					
Research Institute	Chosun University				KARI & KAIST	KAIST & KARI	NRL	University of Sydney	
Price (\$)	38 + $\alpha$	35 + $\alpha$	99 + $\alpha$	399 + $\alpha$	Undefined				
Dimension (cm)	22×12×11	16×12×12	25×16×14	87×47×45					
CPU	Atmel AVR 8-bit ATmega 2560	Quad-core ARM Cortex-A53 @1.2GHz 64-bit Broadcom BCM2837	Quad-core ARM Cortex-A57 @ 1.43 GHz	Quad-core ARM Cortex-A57 @ 2 GHz + Dual-core NVIDIA Denver2 @ 2 GHz					
GPU	-	VideoCore IV	128-core Maxwell	256-core Pascal					
Memory	256 KB Flash 4KB EEPROM 8KB SRAM	1GB LPDDR2	4GB 64-bit LPDDR4	8GB 128-bit LPDDR4					
Storage	MicroSD Card								
Sensor	Current	Blkbox 100A							
	Voltage	In-House Development							
Part	AD Convt	-	MCP3008	MCP3008					HTADC I2C
	MOSFET	IRF4905							
Weight (g)	537	450	598	586					
Nominal Voltage (V)	14.8 (4S)				25.9 (7S)	25.9 (7S)	25.9 (7S)	14.8 (4S)	
Power (W)	770				500	200	Undefined	170	
Max. Flight Time (h)	0.5 (Multicopter) Undefined (Fixed-Wing)				1.5 (Fixed-Wing)	3.8 (Fixed-Wing)	4.5 (Fixed-Wing)	0.3 (Fixed-Wing)	
Appearance									
ROS Capability	O				X	X	O	X	
MAVLINK Communication	O				X				

According to Fig. 10(a), the fluctuation deviation tends to increase with an increase in the environmental temperature, and vice versa, to a good approximation. This is mostly because of the Li-based battery pack characteristics;

that is, the Li-battery pack tends to experience a larger IR drop (or, voltage drop) and smaller capacity as the environmental temperature decreases, and vice versa, as internal resistance increases owing to the slower movement of the

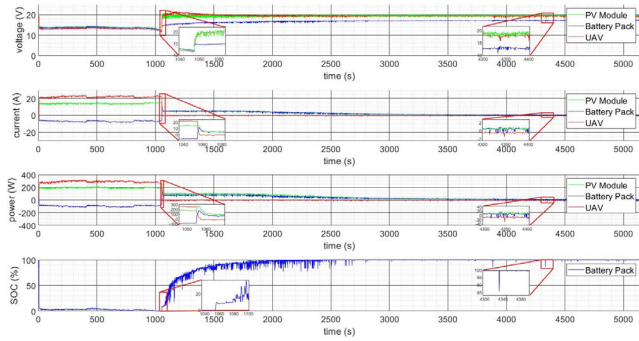


FIGURE 14. Result for RPi-3B-based PMS (w/o supercapacitor).

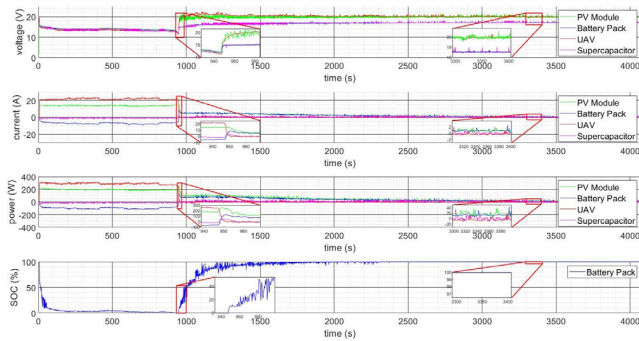


FIGURE 15. Result for RPi-3B-based PMS (w supercapacitor).

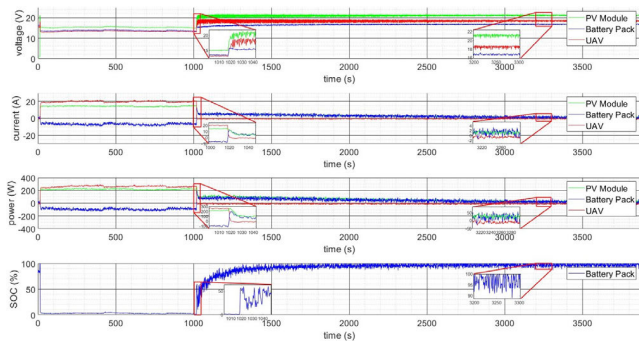


FIGURE 16. Result for NVIDIA-Jetson-Nano-based PMS (w/o supercapacitor).

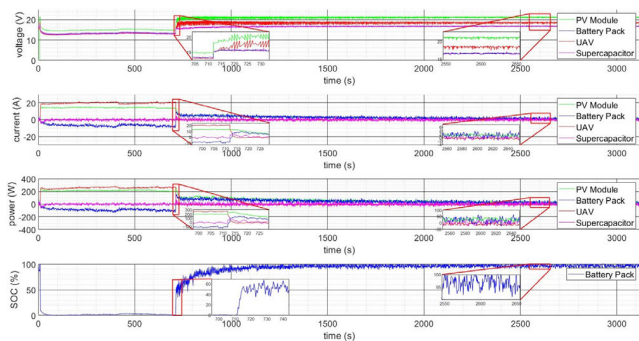


FIGURE 17. Result for NVIDIA-Jetson-Nano-based PMS (w supercapacitor).

Li+ ion. Further, the current and voltage fluctuations occurring at the Li-battery pack affected the inter-connected PV

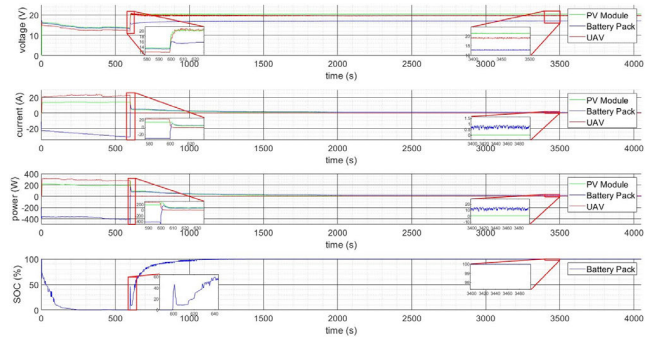


FIGURE 18. Result for NVIDIA-Jetson-TX2-based PMS (w/o supercapacitor).

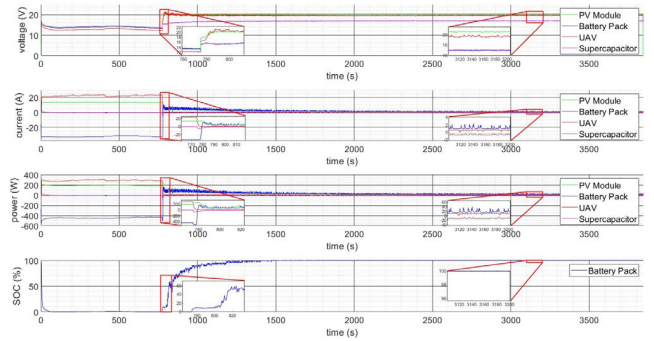


FIGURE 19. Result for NVIDIA-Jetson-TX2-based PMS (w supercapacitor).

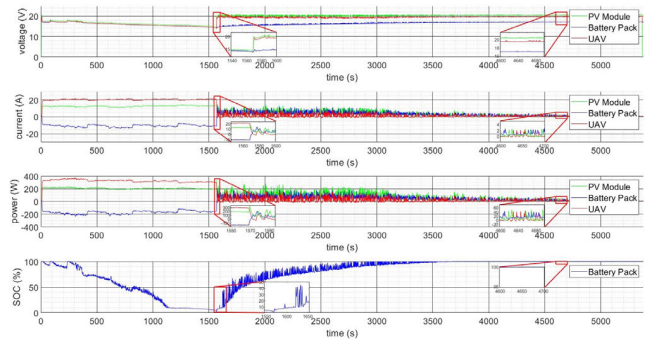


FIGURE 20. Result for Arduino-Mega-based PMS (w/o supercapacitor).

modules and supercapacitor, resulting in the current and voltage fluctuations as well. Moreover, the fluctuation difference among the four PMS prototypes mainly originated from the hardware performance difference determining how precisely the general-purpose input/output (GPIO) signal communication can be controlled.

According to the fluctuation deviation comparison tables, the Jetson Nano exhibited the highest, and the Jetson TX2 the lowest fluctuation deviations. In addition, adding a supercapacitor resulted in a worse fluctuation deviation, which can be attributed to the inherent high C-rate performance capability of the Li-ion battery pack compared to the supercapacitor.

According to Fig. 10(b), the flight time was maximized and minimized at 25 and -10 °C, respectively, when a supercapacitor was connected; however, it was minimized at 40 °C

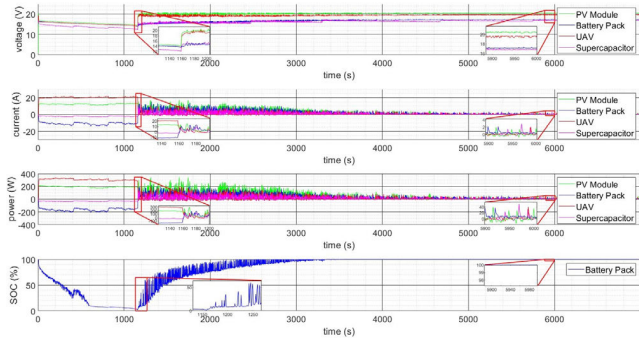


FIGURE 21. Result for Arduino-Mega-based PMS (w supercapacitor).

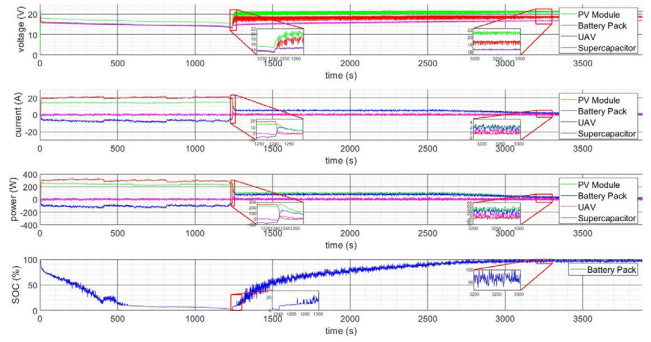


FIGURE 25. Result for NVIDIA-Jetson-Nano-based PMS (w supercapacitor).

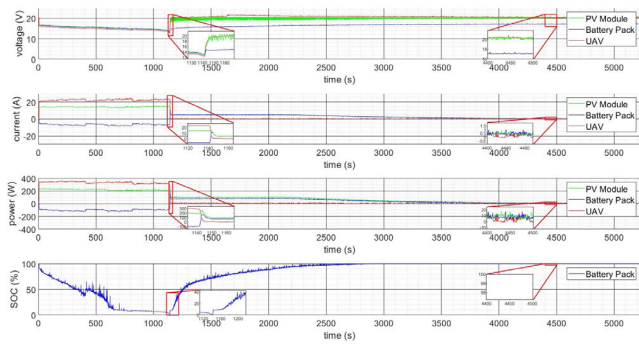


FIGURE 22. Result for RPi-3B-based PMS (w/o supercapacitor).

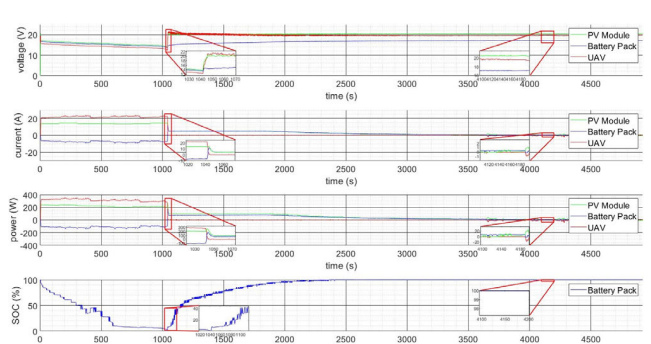


FIGURE 26. Result for NVIDIA-Jetson-TX2-based PMS (w/o supercapacitor).

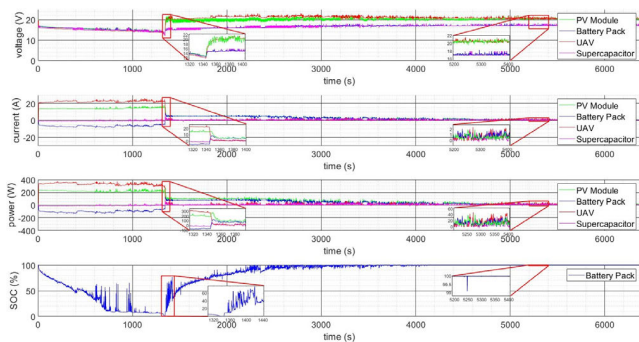


FIGURE 23. Result for RPi-3B-based PMS (w supercapacitor).

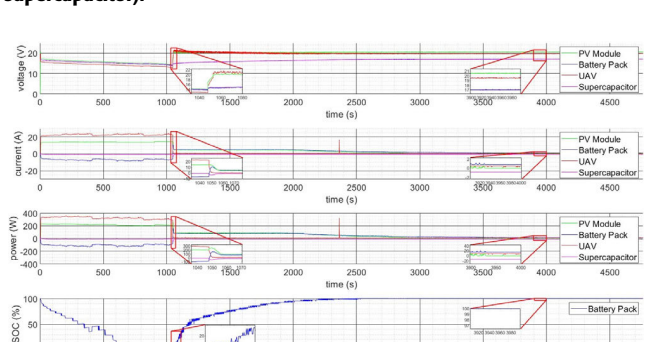


FIGURE 27. Result for NVIDIA-Jetson-TX2-based PMS (w supercapacitor).

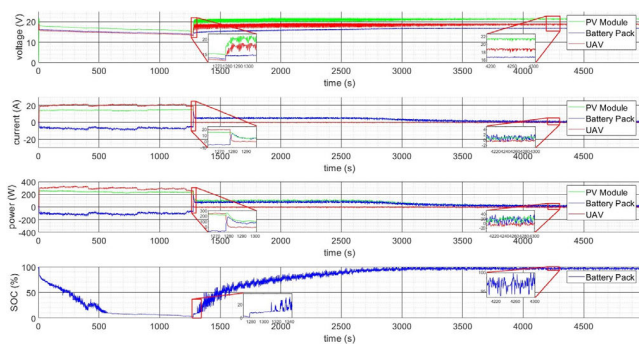


FIGURE 24. Result for NVIDIA-Jetson-Nano-based PMS (w/o supercapacitor).

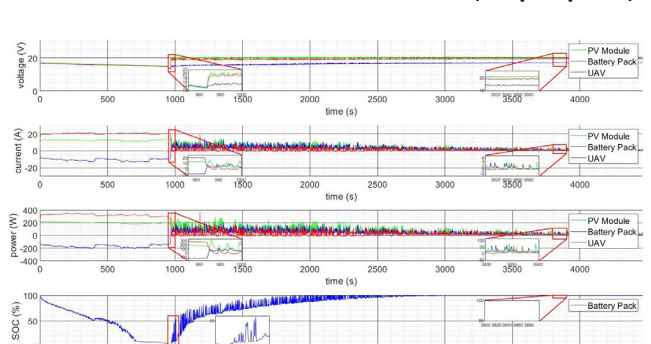


FIGURE 28. Result for Arduino-Mega-based PMS (w/o supercapacitor).

when no supercapacitor was used. This implies that the performance of a supercapacitor varies and greatly affects the

overall performance of the PMS under varying environmental temperatures, and thus, users must be mindful of the

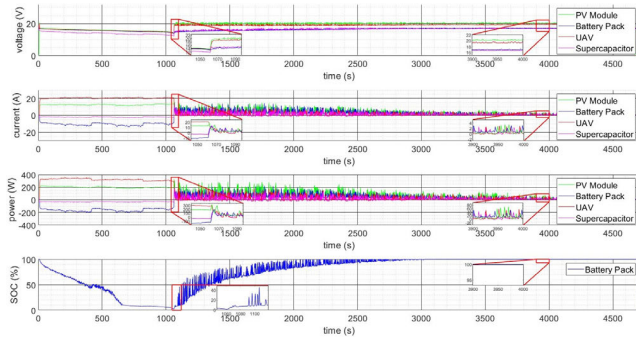


FIGURE 29. Result for Arduino-Mega-based PMS (w supercapacitor).

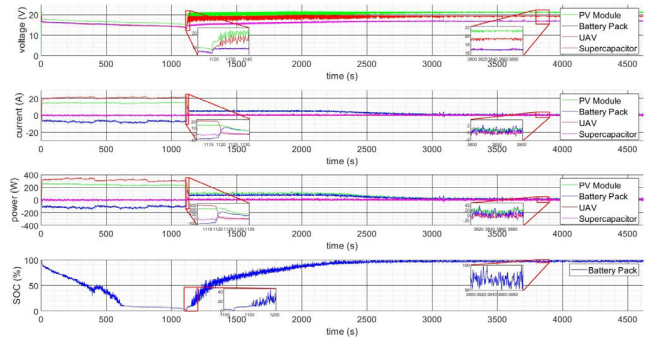


FIGURE 33. Result for NVIDIA-Jetson-Nano-based PMS (w supercapacitor).

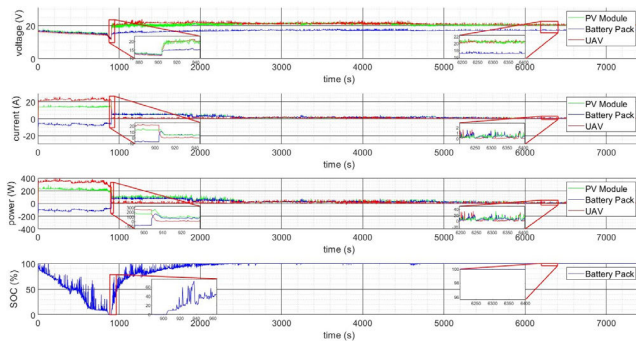


FIGURE 30. Result for RPi-3B-based PMS (w/o supercapacitor).

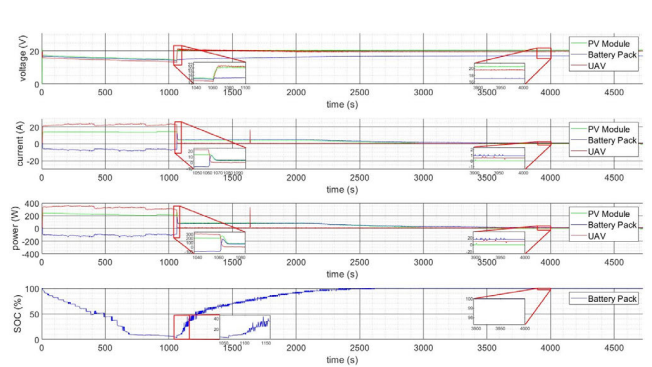


FIGURE 34. Result for NVIDIA-Jetson-TX2-based PMS (w/o supercapacitor).

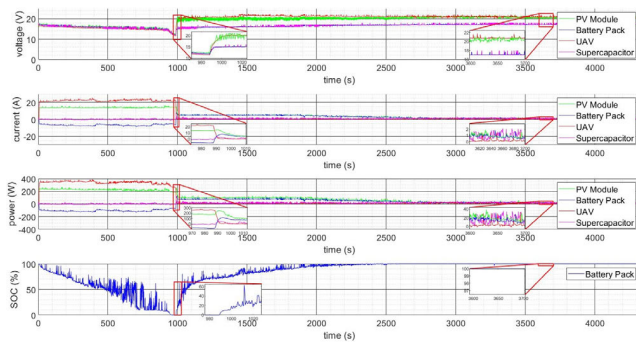


FIGURE 31. Result for RPi-3B-based PMS (w supercapacitor).

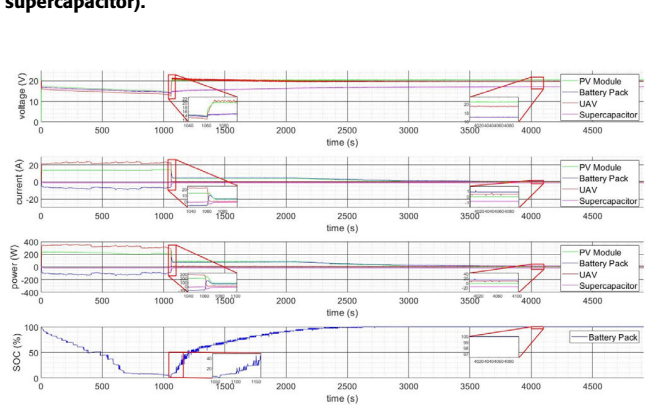


FIGURE 35. Result for NVIDIA-Jetson-TX2-based PMS (w supercapacitor).

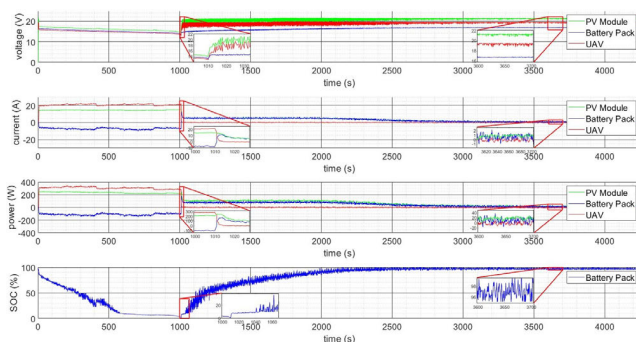


FIGURE 32. Result for NVIDIA-Jetson-Nano-based PMS (w/o supercapacitor).

supercapacitor application. Herein, the fluctuation deviation and flight time were separately investigated because the part

of the CV charging mode was used for the fluctuation deviation analysis and that of the discharging mode for the flight time analysis.

Although the Jetson TX2 exhibited the lowest flight time efficiency, it also showed the lowest functional change between the cases with and without the application of a supercapacitor. Further, the AMega produced the longest flight time in the absence of a supercapacitor, whereas the RPi 3B produced the longest flight time on application of a supercapacitor. Overall, from the user's perspective, the Jetson TX2 is preferred as it exhibits the lowest operational performance differences in the flight time aspect depending on whether the supercapacitor is connected or not.

TABLE 8. Fluctuation deviation comparison (w/o supercapacitor).

	40 °C					25 °C					-10 °C					
	SOC	P	I	V	SOC	P	I	V	SOC	P	I	V	SOC	P	I	V
-	-	11.9	0.59	0.11	-	8.32	0.41	2.75	-	5.56	0.26	0.09	-	-	-	-
0.00	4.76	0.28	0.05	0.04	0.00	4.78	0.28	0.04	0.00	4.71	0.27	0.11	0.00	4.71	0.27	0.11
-	9.90	0.50	0.17	0.44	-	7.38	0.38	0.44	-	4.32	0.21	0.08	-	4.32	0.21	0.08
-	-	-	-	-	-	-	-	-	-	-	-	-	-	-	-	-
-	4.39	0.21	0.24	0.11	-	2.59	0.13	0.11	-	3.21	0.16	0.23	-	3.21	0.16	0.23
0.00	4.80	0.28	0.16	0.07	0.00	2.92	0.17	0.07	0.21	6.27	0.36	0.15	0.21	6.27	0.36	0.15
-	5.75	0.28	0.20	0.17	-	4.44	0.22	0.17	-	3.56	0.19	0.19	-	3.56	0.19	0.19
-	-	-	-	-	-	-	-	-	-	-	-	-	-	-	-	-
-	5.89	0.28	0.12	0.12	-	6.53	0.31	0.12	-	8.61	0.41	0.20	-	8.61	0.41	0.20
1.12	9.64	0.58	0.06	0.06	1.19	11.2	0.67	0.06	2.64	16.7	1.00	0.13	2.64	16.7	1.00	0.13
-	4.74	0.25	0.14	0.16	-	4.74	0.25	0.16	-	6.52	0.35	0.24	-	6.52	0.35	0.24
-	-	-	-	-	-	-	-	-	-	-	-	-	-	-	-	-
-	3.77	0.18	0.06	0.06	-	4.26	0.21	0.06	-	0.48	0.02	0.03	-	0.48	0.02	0.03
0.00	0.48	0.03	0.03	0.06	0.00	0.41	0.02	0.06	0.00	2.13	0.12	0.06	0.00	2.13	0.12	0.06
-	0.87	0.04	0.10	0.04	-	1.55	0.08	0.04	-	0.26	0.01	0.07	-	0.26	0.01	0.07
-	-	-	-	-	-	-	-	-	-	-	-	-	-	-	-	-

V. MILS AND HILS COMPARISON

For the MILS and HILS comparison, the HILS result for the NVIDIA-Jetson-TX2-based PMS with a supercapacitor under 25 °C environmental temperature was used as inputs for the MILS (Fig. 35 in Appendix B). Subsequently, the obtained simulation graphs were overlapped and analyzed for the detailed comparison, as shown in Fig. 11.

Here, the red and blue lines represent the MILS and HILS results, respectively. The power graphs of the motors, PV modules, and battery pack exhibited similar patterns between the MILS and HILS result. The similarity between the MILS and HILS graphs implies that the overall MATLAB/Simulink-based model and its estimated parameters can be utilized for various power flow investigations prior to the actual PMS hardware development. Thus, the MILS and HILS comparison results can aid in pre-checking the PMS operation and outline system concept design.

TABLE 9. Fluctuation deviation comparison (w supercapacitor).

	40 °C					25 °C					-10 °C					
	SOC	P	I	V	SOC	P	I	V	SOC	P	I	V	SOC	P	I	V
-	26.6	1.24	1.01	0.34	0.00	8.08	0.40	0.09	-	9.80	0.46	0.10	-	9.80	0.46	0.10
5.64	16.4	1.01	0.80	2.88	0.00	5.05	0.29	0.04	1.38	6.59	0.38	0.26	1.38	6.59	0.38	0.26
-	20.7	0.80	0.85	0.51	-	6.99	0.36	0.12	-	7.45	0.36	0.07	-	7.45	0.36	0.07
-	14.46	0.85	0.26	0.27	-	5.52	0.33	0.05	-	6.25	0.38	0.07	-	6.25	0.38	0.07
-	5.17	0.26	0.27	0.12	-	5.08	0.25	0.20	-	5.28	0.26	0.22	-	5.28	0.26	0.22
0.00	4.66	0.27	0.12	0.00	0.00	4.68	0.27	0.14	0.00	3.96	0.23	0.13	0.00	3.96	0.23	0.13
-	5.37	0.26	0.15	0.15	-	6.78	0.33	0.16	-	5.43	0.27	0.12	-	5.43	0.27	0.12
-	8.25	0.48	0.18	0.18	-	5.55	0.33	0.16	-	9.85	0.58	0.19	-	9.85	0.58	0.19
-	5.85	0.28	0.13	0.13	-	8.02	0.38	0.22	-	9.95	0.47	0.19	-	9.95	0.47	0.19
1.11	10.0	0.60	0.05	0.05	1.40	11.5	0.69	0.07	2.31	17.1	1.03	0.12	2.31	17.1	1.03	0.12
-	4.45	0.23	0.15	0.15	-	4.74	0.25	0.28	-	6.34	0.34	0.24	-	6.34	0.34	0.24
-	10.41	0.62	0.14	0.14	-	10.63	0.64	0.10	-	18.2	1.09	0.15	-	18.2	1.09	0.15
-	3.85	0.19	0.06	0.06	-	1.59	0.08	0.06	-	0.86	0.04	0.19	-	0.86	0.04	0.19
0.00	0.68	0.04	0.03	0.03	0.00	0.88	0.05	0.03	0.00	4.83	0.28	0.05	0.00	4.83	0.28	0.05
-	0.81	0.04	0.08	0.08	-	1.33	0.07	0.08	-	1.53	0.08	0.22	-	1.53	0.08	0.22
-	0.01	0.00	0.01	0.01	-	0.01	0.00	0.01	-	2.28	0.13	0.05	-	2.28	0.13	0.05

VI. CONCLUSION

In this study, four different PMS prototypes were developed and compared using MILS and HILS under varying environmental temperatures, with respect to the presence or absence of a supercapacitor.

According to the experimental results, in general, the supercapacitor application resulted in poor performance in terms of the in-flow current fluctuation deviation into and out of the battery pack during the end of the constant current and constant voltage charging process. This was mainly attributed to the Li-ion battery pack’s high C-rate performance capability comparable to the supercapacitor. Further, among the four PMS candidates, the Jetson TX2 exhibited the best functionality in terms of power management, whereas AMega was best in terms of energy management.

**TABLE 10. Fluctuation deviation comparison for tests w/o and w/ supercapacitor.**

	AMega				RPi 3B				Jetson Nano				Jetson TX2			
	PV	Bat	UAV	S-Cap	PV	Bat	UAV	S-Cap	PV	Bat	UAV	S-Cap	PV	Bat	UAV	S-Cap
-10 °C	V	-	-	0.01	-	0.01	0.02	0.07	-	0.01	0.01	0.00	-	-	0.01	-
	I	-	-	-	-	0.13	-	-	-	-	0.01	-	-	-	-	-
	P	-4.24	-1.88	-3.13	-	-2.07	2.31	-1.87	-	-1.34	-0.41	0.18	-	-0.38	-2.7	-1.27
	SOC	-	-1.38	-	-	-	0.21	-	-	-	0.33	-	-	-	0.00	-
25 °C	V	2.66	0.00	0.32	-	-0.09	-0.07	0.01	-	-0.10	-0.01	-0.12	-	0.00	0.03	-0.04
	I	0.01	-0.01	0.02	-	-0.12	-0.10	-0.11	-	-0.07	-0.02	0.00	-	0.13	-0.03	0.01
	P	0.24	-	0.39	-	-	-	-	-	-	0.00	-	-	2.67	-	0.22
	SOC	-	0.00	-	-	-	0.00	-	-	-	-0.21	-	-	0.00	-	-
40 °C	V	-1.09	-0.29	-2.71	-	0.12	0.04	0.05	-	-0.01	0.01	-0.01	-	0.00	0.00	0.02
	I	-0.65	0.73	-0.30	-	-0.05	0.01	0.02	-	0.00	-0.02	0.02	-	-0.01	-0.01	0.00
	P	-14.64	-11.69	-10.86	-	-0.78	0.14	0.38	-	0.04	-0.42	0.29	-	-0.08	-0.20	0.06
	SOC	-	-5.64	-	-	-	-	-	-	0.01	-	-	-	0.00	-	-

**TABLE 11. Flight time comparison (w/o supercapacitor).**

	AMega	RPi 3B	Jetson Nano	Jetson TX2
-10 °C	1165.4	1055	1018	600
25 °C	1568.4	1142	1278	1042
40 °C	967.6	904	1010	1061

Although previous meaningful results were observed, they have limitations in that they were obtained from indoor HILS tests rather than real flight tests. Nevertheless, the MILS and

**TABLE 12. Flight time comparison (w supercapacitor).**

	AMega	RPi 3B	Jetson Nano	Jetson TX2
-10 °C	664.6	947	712	775
25 °C	1158.8	1345	1241	1048
40 °C	1061.6	988	1119	1061

**TABLE 13. Flight time differentials for tests w/o and w/ supercapacitor.**

	AMega	RPi 3B	Jetson Nano	Jetson TX2
-10 °C	500.8	108	306	-175
25 °C	409.6	-203	37	-6
40 °C	-94	-84	-109	0

HILS yielded meaningful discoveries, which may advance the technology of hybrid-powered UAVs.

In the future, an upgraded Jetson-TX2-based PMS will be developed as a multilayer PCB and installed in the UAS to perform outdoor flight experiments. The power interflows occurring in the PMS at different weather conditions is necessary as it aids in the validation of the research motivation. Further, it highlights the significance of the experimental results presented in this manuscript.

**VII. APPENDIX A**

See Table 7.

**VIII. APPENDIX B**

**A. AMBIENT TEMPERATURE: -10°**

See Figs. 12–19.

**B. AMBIENT TEMPERATURE: 25°**

See Figs. 20–27.

**C. AMBIENT TEMPERATURE: 40°**

See Figs.28–35.

**IX. APPENDIX C**

**A. FLUCTUATION DEVIATION COMPARISON**

See Tables 8–10.

**B. FLIGHT TIME COMPARISON**

See Tables 11–13.

**REFERENCES**

- [1] Y. Huang, H. Wang, and P. Yao, "Energy-optimal path planning for solar-powered UAV with tracking moving ground target," *Aerosp. Sci. Technol.*, vol. 53, pp. 241–251, Jun. 2016.
- [2] Y. Huang, J. Chen, G. Su, H. Wang, R. Liu, and P. Du, "Energy-optimal path planning for solar-powered UAVs monitoring stationary target," in *Proc. 4th ACM SIGSPATIAL Int. Workshop Saf.*, Nov. 2018, pp. 1–8.
- [3] H. Huang, A. V. Savkin, and W. Ni, "Energy-efficient 3D navigation of a solar-powered UAV for secure communication in the presence of eavesdroppers and no-fly zones," *Energies*, vol. 13, no. 1445, pp. 1–12, Mar. 2020.

- [4] J. Wu, H. Wang, N. Li, P. Yao, Y. Huang, and H. Yang, "Path planning for solar-powered UAV in urban environment," *Neurocomputing*, vol. 275, pp. 2055–2065, Jan. 2018.
- [5] J. Wu, H. Wang, Y. Huang, Z. Su, and M. Zhang, "Energy management strategy for solar-powered UAV long-endurance target tracking," *IEEE Trans. Aerosp. Electron. Syst.*, vol. 55, no. 4, pp. 1878–1891, Aug. 2019.
- [6] J. Wu, H. Wang, Y. Huang, M. Zhang, and Z. Su, "Solar-powered aircraft endurance map," *J. Guid., Control, Dyn.*, vol. 42, no. 3, pp. 687–694, Mar. 2019.
- [7] H. He, R. Xiong, K. Zhao, and Z. Liu, "Energy management strategy research on a hybrid power system by hardware-in-loop experiments," *Appl. Energy*, vol. 112, pp. 1311–1317, Dec. 2013.
- [8] H. Tazvinga, B. Zhu, and X. Xia, "Energy dispatch strategy for a photovoltaic-wind-diesel-battery hybrid power system," *Sol. Energy*, vol. 108, pp. 412–420, Oct. 2014.
- [9] Y. Huang, H. Wang, N. Li, and Y. Yu, "Endurance estimate for solar-powered unmanned aerial vehicles," in *Proc. 9th Int. Conf. Intell. Human-Machine Syst. Cybern. (IHMSC)*, vol. 1, Aug. 2017, pp. 66–70.
- [10] X. Zhang, L. Liu, Y. Dai, and T. Lu, "Experimental investigation on the online fuzzy energy management of hybrid fuel cell/battery power system for UAVs," *Int. J. Hydrogen Energy*, vol. 43, no. 21, pp. 10094–10103, May 2018.
- [11] X. Zhang, L. Liu, and Y. Dai, "Fuzzy state machine energy management strategy for hybrid electric UAVs with pv/fuel cell/battery power system," *Int. J. Aerosp. Eng.*, vol. 2018, pp. 1–16, Jul. 2018.
- [12] K. N. Mobariz, A. M. Youssef, and M. Abdel-Rahman, "Long endurance hybrid fuel cell-battery powered UAV," *World J. Model. Simul.*, vol. 11, no. 1, pp. 69–80, Jan. 2015.
- [13] J.-K. Shiau, Y.-C. Wei, and M.-Y. Lee, "Fuzzy controller for a voltage-regulated solar-powered MPPT system for hybrid power system applications," *Energies*, vol. 8, no. 5, pp. 3292–3312, Apr. 2015.
- [14] A. Gong, D. Verstaete, and J. L. Palmer, "Evaluation of a hybrid fuel-cell based propulsion system with a hardware-in-the-loop flight simulator," in *Proc. 23rd Int. Soc. Air-Breathing Engines Conf.*, Sep. 2017, pp. 1–17.
- [15] B. G. Gang and S. Kwon, "Design of an energy management technique for high endurance unmanned aerial vehicles powered by fuel and solar cell systems," *Int. J. Hydrogen Energy*, vol. 43, no. 20, pp. 9787–9796, May 2018.
- [16] A. Gong, J. L. Palmer, and D. Verstaete, "Flight test of a fuel-cell/battery/supercapacitor triple hybrid UAV propulsion system," in *Proc. 31st Congr. Int. Council Aeronaut. Sci.*, Sep. 2018, pp. 1–10.
- [17] A. Malaver, N. Motta, P. Corke, and F. Gonzalez, "Development and integration of a solar powered unmanned aerial vehicle and a wireless sensor network to monitor greenhouse gases," *Sensors*, vol. 15, no. 2, pp. 4072–4096, Feb. 2015.
- [18] P. Oettershagen, A. Melzer, T. Mantel, K. Rudin, T. Stastny, B. Wawrzacz, T. Hinzmann, S. Leutenegger, K. Alexis, and R. Siegwart, "Design of small hand-launched solar-powered UAVs: From concept study to a multi-day world endurance record flight," *J. Field Robot.*, vol. 34, no. 7, pp. 1352–1377, May 2017.
- [19] J.-K. Shiau and D.-M. Ma, "Development of an experimental solar-powered unmanned aerial vehicle," *J. Chin. Inst. Engineers*, vol. 38, no. 6, pp. 701–713, Mar. 2015.
- [20] R. O. Stromann, D. J. Edwards, P. Jenkins, S. Carter, D. Newton, M. Kelly, S. Heinzen, T. Young, V. N. Dobrokhodov, J. Langelaan, J. Bird, and P. A. Reinecke, "The hybrid tiger: A long endurance solar/fuel cell/soaring unmanned aerial vehicle," in *Proc. 48th Power Sources Conf.*, Jun. 2018, pp. 1–14.
- [21] C. Yang, S. Moon, and Y. Kim, "A fuel cell/battery hybrid power system for an unmanned aerial vehicle," *J. Mech. Sci. Technol.*, vol. 30, no. 5, pp. 2379–2385, May 2016.
- [22] M. N. Boukoberine, Z. Zhou, and M. Benbouzid, "A critical review on unmanned aerial vehicles power supply and energy management: Solutions, strategies, and prospects," *Appl. Energy*, vol. 255, no. 1, pp. 1–22, Dec. 2019.
- [23] T. Lei, Z. Yang, Z. Lin, and X. Zhang, "State of art on energy management strategy for hybrid-powered unmanned aerial vehicle," *Chin. J. Aeronaut.*, vol. 32, no. 6, pp. 1488–1503, Jun. 2019.
- [24] V. Verdingovas, M. S. Jellesen, and R. Ambat, "Impact of NaCl contamination and climatic conditions on the reliability of printed circuit board assemblies," *IEEE Trans. Device Mater. Rel.*, vol. 14, no. 1, pp. 42–51, Mar. 2014.
- [25] J. Coonrod, "Thermal design begins at the circuit board," *Microw. RF*, vol. 50, no. 5, p. 33, May 2011.
- [26] L. Michaels, S. Pagerit, A. Rousseau, P. Sharer, S. Halbach, R. Vijayagopal, M. Kropinski, G. Matthews, M. Kao, O. Matthews, and M. Steele, "Model-based systems engineering and control system development via virtual hardware-in-the-loop simulation," Argonne Nat. Lab., Lemont, IL, USA, SAE Tech. Rep. 2010-01-2325, Nov. 2010.
- [27] J.-K. Shiau, D.-M. Ma, P.-Y. Yang, G.-F. Wang, and J. Hua Gong, "Design of a solar power management system for an experimental UAV," *IEEE Trans. Aerosp. Electron. Syst.*, vol. 45, no. 4, pp. 1350–1360, Oct. 2009.
- [28] A. V. Bystrov, V. Golubev, F. Zagumennov, A. Varyukhin, and V. Merzlikin, "The development of hybrid power management unit for unmanned aerial vehicles," in *Proc. IEEE Int. Conf. Archit., Construction, Environ. Hydraul. (ICACEH)*, Dec. 2019, pp. 141–144.
- [29] B. Lee, S. Kwon, P. Park, and K. Kim, "Active power management system for an unmanned aerial vehicle powered by solar cells, a fuel cell, and batteries," *IEEE Trans. Aerosp. Electron. Syst.*, vol. 50, no. 4, pp. 3167–3177, Oct. 2014.
- [30] K. Zachariadou, K. Yiasemides, and N. Trougakos, "A low-cost computer-controlled Arduino-based educational laboratory system for teaching the fundamentals of photovoltaic cells," *Eur. J. Phys.*, vol. 33, no. 6, pp. 1599–1610, Sep. 2012.
- [31] S. Jung and H. Jeong, "extended Kalman filter-based state of charge and state of power estimation algorithm for unmanned aerial vehicle Li-Po battery packs," *Energies*, vol. 10, p. 1237, Aug. 2017.
- [32] M. C. Argyrou, P. Christodoulides, C. C. Marouchos, and S. A. Kalogirou, "Hybrid battery-supercapacitor mathematical modeling for PV application using MATLAB/Simulink," in *Proc. 53rd Int. Universities Power Eng. Conf. (UPEC)*, Sep. 2018, pp. 1–6.
- [33] D. L. Gabriel, J. Meyer, and F. D. Plessis, "Brushless DC motor characterisation and selection for a fixed wing UAV," in *Proc. IEEE Africon*, Sep. 2011, pp. 1–6.



**SUNGHUN JUNG** (Member, IEEE) received the B.S. degree from the University of Minnesota, Twin Cities, USA, in 2009, and the M.S. and Ph.D. degrees from Purdue University, West Lafayette, USA, in 2010 and 2013, respectively, all in mechanical engineering.

He was a Principal Researcher with Samsung SDI, from 2014 to 2016. He has been an Assistant Professor with the Faculty of Smart Vehicle System Engineering, Chosun University. His research interest includes control and optimization for autonomous operations of unmanned assets, particularly UAVs.



**YOUNG-JOON KIM** (Member, IEEE) received the B.S. and M.S. degrees in electrical engineering from the Korea Advanced Institute of Science and Technology, Daejeon, Republic of Korea, in 2008 and 2010, respectively, and the Ph.D. degree in electrical and computer engineering from Purdue University, West Lafayette, USA, in 2016.

He joined Samsung Research, Samsung Electronics, Suwon, Republic of Korea, in 2016, where he has involved in wireless power transfer and energy harvesting. Since 2018, he has been an Assistant Professor with the Department of Electronic Engineering, Gachon University. His research interests include mm-wave devices, wireless power transfer, and biomedical sensor networks.

...